energies

MDPI

Article

Experimental and Analytical Investigation of an Immiscible Displacement Process in Real Structure Micromodels

Christian Truitt Lüddeke *,†, Calvin Lumban Gaol ‡, Gion Joel Strobel ‡ and Leonhard Ganzer ‡

Institute of Subsurface Energy Systems, Clausthal University of Technology, 38678 Clausthal-Zellerfeld, Germany
* Correspondence: christian.truitt.lueddeke@tu-clausthal.de
† Current address: Agricolastrasse 10, 38678 Clausthal-Zellerfeld, Germany.
‡ These authors contributed equally to this work.

Abstract: The recovery of oil from a reservoir can be accomplished with various methods, one of the most commonly applied types being waterflooding. A common theory used to describe immiscible displacement is the Buckley–Leverett theory. A brand new type of micromodel, generated and fabricated by using a micro-computer tomography (μCT) image stack of a real sandstone core, was used to conduct immiscible displacement experiments. Critical logging data were recorded, and a high-resolution camera took pictures of the displacement process. In an image processing tool (MATLAB), an algorithm was developed to evaluate the pictures of the experiment and to examine the changes in the saturations of the displacing and the displaced fluid. The main objective of the displacement experiment was to validate the new microchip in two-phase displacement experiments and to assess the feasibility of the image processing algorithm. This was performed by comparing the results of the experimental to the analytical solutions, which were derived from the Buckley–Leverett theory. The comparison of the results showed a good match between the two types of solutions. The applicability of the analytical results to the experimental procedures was observed. Additionally, the usage of the newly fabricated micromodel and its potential to visualize the fluid flow behavior in porous media were assessed.

Keywords: microfluidic devices; immiscible displacement; waterflooding; Buckley–Leverett

Citation: Lüddeke, C.T.; Gaol, C.L.; Strobel, G.J.; Ganzer, L. Experimental and Analytical Investigation of an Immiscible Displacement Process in Real Structure Micromodels. *Energies* **2022**, *15*, 6741. https://doi.org/10.3390/en15186741

Academic Editor: Rouhi Farajzadeh

Received: 23 August 2022
Accepted: 11 September 2022
Published: 15 September 2022

1. Introduction

The production of oil from a reservoir is a process that has been performed and improved over many decades. Over time, the depths from which oil has been recovered have increased steadily. Many technologies and methods have been invented and perfected to produce as much oil as possible. The production of oil can be divided into three main methods: primary recovery, secondary recovery, and tertiary recovery. During primary recovery, the natural reservoir pressure is sufficient for the oil to flow through the reservoir to the well. When the natural overpressure declines, then secondary recovery methods such as waterflooding or gas injection are applied to displace the oil from the porous media. Tertiary recovery methods are applied when the secondary recovery methods are no longer feasible or efficient. Secondary recovery methods include the key technique of waterflooding in order to increase the amount of the recovered oil. The theory on immiscible waterflooding, in which a fluid initially in place in a porous media is displaced by an injected fluid, was first described by S.E. Buckley and M.C. Leverett in 1942 [1]. In the Buckley–Leverett theory, the displacing fluid is a constant front as is permeates through the porous media. One essential characteristic of the theory is that is assumes that the displacement occurs in one dimension. The depiction of this process is also known as the frontal advance equation (FAD), and it can be portrayed as a frontal advance displacement graph.

For many decades, numerous experiments and works have been conducted to evaluate the efficiency of waterflooding processes in reservoir rocks at various scales. Starting

from the pore scale at which micromodels are used, experiments and analysis have also been conducted in core-plugs at a core scale and simulations have been performed to evaluate waterflooding processes at a field scale. The principle of waterflooding is not new and has been applied for many years. Babson et al. drilled an injection well and conducted a waterflooding process in the Richfield field in California to observe the impact of waterflooding on the oil and water production [2].

At a core scale, Breston and Hughes conducted waterflooding experiments with brine at different injection rates on two cores. Their aim was to determine the impact of the different flow rates on the oil recovery and on the levels of residual oil saturation [3]. Johnston and van Wingen performed waterflooding experiments on high-permeability unconsolidated core samples, which were mainly heavy oil sands [4]. Talash and Crawford investigated the effects of the initial saturation, viscosity, and wettability on oil recovery from waterflooding [5]. Zhang and Sun developed a method that reliably and quickly calculated the equilibrium properties of unconventional reservoirs including capillary pressures, which contributed to the physical models used to simulate subsurface multiphase flow [6]. Furthermore, Zhang and Sun developed a simulation method using a lattice Boltzmann method to incorporate, on one scale, the free flow of gas in conventional pore channels and, on the second scale, the diffusion of gas, including dynamic sorption, in very narrow pores in the tight matrix in shale reservoirs. With this model, an analysis of the interaction of gas transport and the flow of gas on both scales was analyzed [7].

At a pore scale, micromodels were first considered more than 60 years ago to investigate fluid behavior in porous media [8]. Kargozarfard et al. conducted immiscible displacement experiments in a Hele-Shaw model to visualize and evaluate the influence of viscous fingers on the areal sweep efficiency and on the oil recovery factor [9]. Wegner used glass–silicon–glass micromodels to investigate the recovery of oil when polymers were used in the displacement process to obtain a better understanding of the influences on the rock properties [10]. More recently, Gaol et al. developed a new glass–silicon–glass micromodel, which was designed based on a μCT image stack of a real sandstone core [11]. The new micromodel replicated the internal porous structure of the sandstone core, and a waterflooding experiment was performed with the designed microchip. The detailed development of such micromodels was described in [11]. Results obtained with this new micromodel enable upscaling of the collected flow properties from a micromodel to a core scale. However, little attention has been paid to a direct comparison of the analytical results derived in the Buckley–Leverett theory and experimental immiscible two-phase displacement processes in a brand-new constructed micromodel, which has been developed to replicate the properties and features of a genuine sandstone core.

The goal of this work is to perform a validation of the brand-new developed micromodel by conducting immiscible two-phase displacement experiments and comparing the experimental results to analytically developed solutions. The micromodels used have an internal porous structure that was generated based on a new algorithm, which conducts micro-CT imaging on a Bentheimer sandstone. Five assumptions ensure the validity of the Buckley–Leverett theory, namely immiscibility, incompressibility of the two phases, laminar flow, displacement in one dimension, and neglecting capillary pressure. For simplification, the capillary pressure was neglected. However, capillary pressure should be considered as two phases were present in the micromodel during the experiment. The development of the oil and water saturations and the behavior of the displacement front were observed. A new algorithm for an image processing tool was developed to facilitate the observation of the variation of saturations in the micromodel. The following parameters were measured and used for the comparison: absolute water permeability k, relative permeability endpoints $k_{r,e}$, the saturations of oil and water, their viscosities μ, and the breakthrough time t_{Bt}. The results of the experiment, especially the relevant saturations and the recovery factor, were analyzed, and analytical Buckley–Leverett solutions were developed and compared to the experimental solutions.

2. Materials and Methods

2.1. Experimental Setup

The immiscible displacement experiments were conducted in a microfluidic setup. The setup of the experiment is very similar to the one described in [11,12], and it is depicted in the following Figure 1.

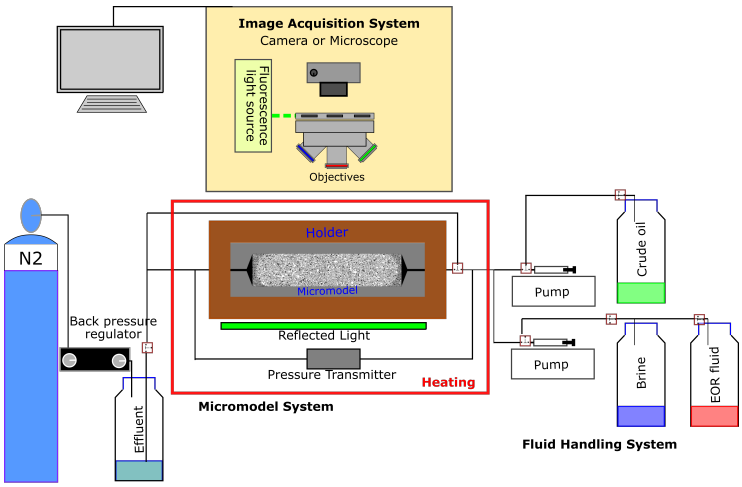

Figure 1. Sketch of the general available experimental setup, which consists of three main components: the fluid handling, the micromodel, and the image acquisition system.

The setup consisted of three main components: the pump, the fluid handling system, and effluent containers. To conduct the experiments, one Harvard Pump 11 Elite Series syringe was filled with distilled water and another one was filled with crude oil. Both syringes were installed in the pump. The high-resolution Nikon camera was part of the image acquisition system of the setup, and it was used to capture images of the displacement process. This camera was focused on the entire area of the micromodel. This enabled the observation of the displacement process in the whole micromodel.

The third part of the setup was the micromodel holder, which contained the microchip. This holder along with the micromodel was placed directly below the camera, and it was connected with the flow lines. An absolute pressure sensor was installed just before the inlet of the holder to measure the inlet pressure. Close to the outlet of the holder, another absolute pressure sensor was installed. The measurement of the differential pressure in the microchip was conducted by determining the difference in the pressure values between the two sensors. The experiment was carried out at a standard room temperature of 22 °C, and a backpressure of 1.9 bar(g) was applied to the system. This level of backpressure was selected to ensure that the microchip was free of any gas bubbles. The micromodel holder was positioned on the surface of a heating plate. If desired, the heating plate can apply temperatures of up to nearly 100 °C to the microchip. Below the micromodel holder, a reflected bottom light was present. This light was used to monitor the saturations for both water and oil and to distinguish between the two fluids.

2.2. Micromodels

The microchip used was made of a glass–silicon–glass structure with a length of 50 mm, a width of 9 mm, and a height distance of 50 µm between the two glass layers. The wettability of the micromodel's internal structure was water-wet. The novelty of this microchip is a new development approach. The micromodel is a replicate of a Bentheimer core plug. First, numerous 2D images were taken of the core plug using μCT images to develop a high-quality 3D image stack. Then, a digital rock physics method was applied to determine the rock properties of the micromodel, for instance absolute permeability and porosity. An identical method was applied to determine the distribution of the grain sizes

and to determine the flow channels. Combining all the processes resulted in replicating the core plug properties in the micromodel. At each end of the micromodel, artificial flow channels that connect the inlet and the outlet of the micromodel with the internal structure were added. The artificial flow channels were intended to provide a more uniform, homogeneous flow of the fluids into and through the micromodel. The detailed process of the development is described in [11]. The used micromodel is similar to the one mentioned in [11,13], and the structure of the microchip is shown in the following Figure 2.

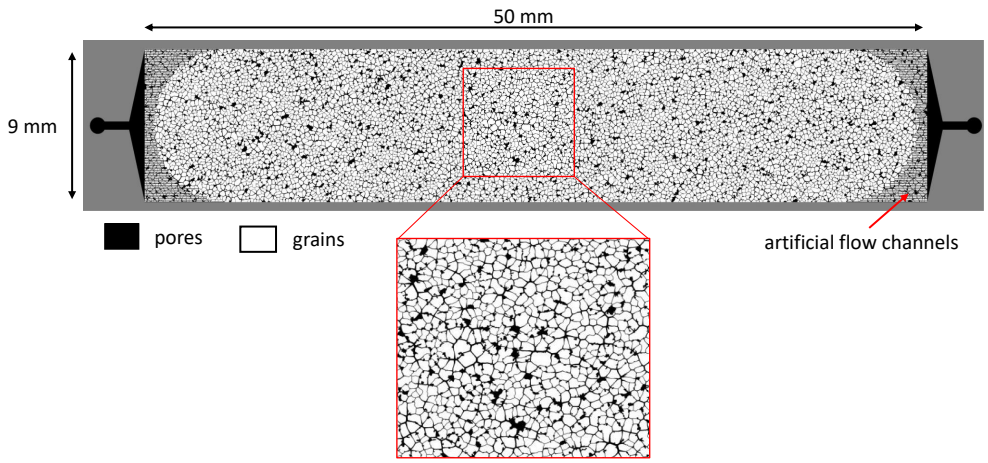

Figure 2. Structure of a microchip: The black color indicates the pores, flow channels and inlet and outlet boreholes. The white color represents the grains.

The micromodel shown in Figure 2 shows the result of the development procedure described above. The boreholes at the very left and right of the microchip are represented by the black points, which are connected to the artificial flow channels. The displayed micromodel has a homogeneous permeability distribution in the entire area of the microchip. The microchip, which was used in the experiment described in this paper, was developed with the same method. The development and fabrication of this micromodel would permit an easier upscaling of fluid flow behavior to larger scales. The provided value for the absolute permeability of the microchip used in the experiment was 2000 mD. The mean pore size of the pore throats was 46.42 µm, and the average porosity was 0.24 [11].

2.3. Experimental Procedure

Before the experiments were conducted, the microchips were thoroughly cleaned on the inside with high injection rates of isopropanol and distilled water to remove any kind of residue or gas bubbles. To ensure that no gas remained in the micromodel, a backpressure of 2 bar(g) was applied. After this cleaning process, the micromodel was completely saturated with distilled water. The first measurements that were performed were to determine the absolute permeability of the internal structure of the microchip. The measured permeability value was needed for the relative permeability endpoint calculations and to assess the cleanliness of the micromodel structure. These measurements were performed by applying a constant injection rate to the syringe pump, which was filled with distilled water, and injecting the water through the flow line into the micromodel. The rate of the injection was kept stable and the differential pressure between the inlet and the outlet was observed until it stabilized. After it had stabilized, the measured differential pressure was used to calculate the permeability with Darcy's law. In total, three different injection rates were applied to obtain a reliable value for the measured permeability.

After concluding the permeability measurement, the microchip was saturated with oil. The injected oil had a viscosity of 7.55 cP at room temperature. The oil saturation process was conducted at five different consecutive flow rates. Each flow rate was applied to the syringe pump and maintained while the oil was flowing through the micromodel. For each flow rate, the differential pressure between the inlet and the outlet was measured. In total,

five injection rates were applied. The first flow rate (0.03 µL/min), which was equivalent to interstitial velocity, lasted for approximately six hours. This was followed by three bump rates (1 µL/min, 5 µL/min, 10 µL/min), which lasted for four hours each. The last injection rate (0.1 µL/min) was applied for a time span of two hours.

The final pressure reading after the last time step was used to calculate the endpoint relative permeability for the analytical solution and the mobility ratio. The respective injection rate was kept at a constant level until the saturations of oil (S_o) and water (S_w) remained stable, which was validated with image analysis. During the injection process, the changes in the saturations of oil and water were observed. For every step of the injection process, images of the microchip were taken and used to determine the saturations. Each image was analyzed with the newly developed algorithm in the image processing tool MATLAB. An image of this microchip saturated with oil (brown) and water (white) can be seen in the following Figure 3.

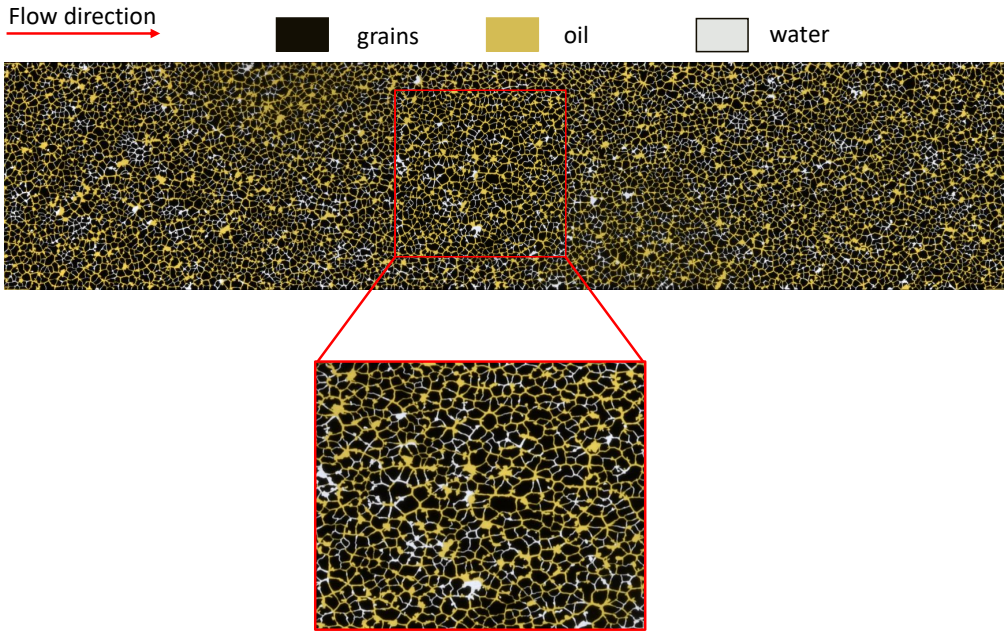

Figure 3. Saturated microchip: black indicates the grains; brown represents oil; white indicates water.

The next steps involved changing the injection fluid from oil to distilled water in order to start the waterflooding process. The injection of water started at a flow rate of 0.03 µL/min, which corresponded to a flow rate of 0.3 ft/d [11]. This flow rate was chosen because it was intended to represent an injection rate in a real-life waterflooding process in a reservoir. Natural flow rates are below 1 ft/d. The applied value for the experimental waterflooding process of 0.03 µL/min was an acceptable value. This flow rate indicated laminar flow inside the micromodel, which is an essential characteristic to perform the experiments according to Gaol et al. [14]. During the water displacement process, the high-resolution Nikon camera in the experimental setup regularly took images of the entire micromodel in a time sequence of every 60 s. These images showed the changes of the saturations of both fluids over time. During the entire process of waterflooding, four different flow rates were applied to the microchip just like during the oilflooding process mentioned earlier. The objective was to measure the differential pressure and to determine the relative permeability endpoints, first for oil and, later on, for water. The change to the subsequent flow rate was completed after the saturation of both fluids remained constant during the previous flow rate. In every step of the waterflooding process, the differential pressure data were measured and the changes in the water and oil saturations

were determined. After the waterflooding process had ended, the inside of the micromodel was cleaned with high-rate injections of distilled water and isopropanol.

2.4. Image Analysis

The images taken during the waterflooding experiment were imported and analyzed by the image processing tool MATLAB. An algorithm was developed that processed the images and evaluated the saturations for oil, water, and the respective changes. The algorithm was also developed to indicate changes in saturations not only in the entire microchip, but also in local segments of the model. This was performed to analyze the flow of the waterfront and to determine its location in the microchip.

Additionally, with the help of the tool and the developed algorithm, the respective times at which these particular saturations were detected in the microchip globally and locally were determined. The following Figure 4 shows the procedure of processing an image of this experiment.

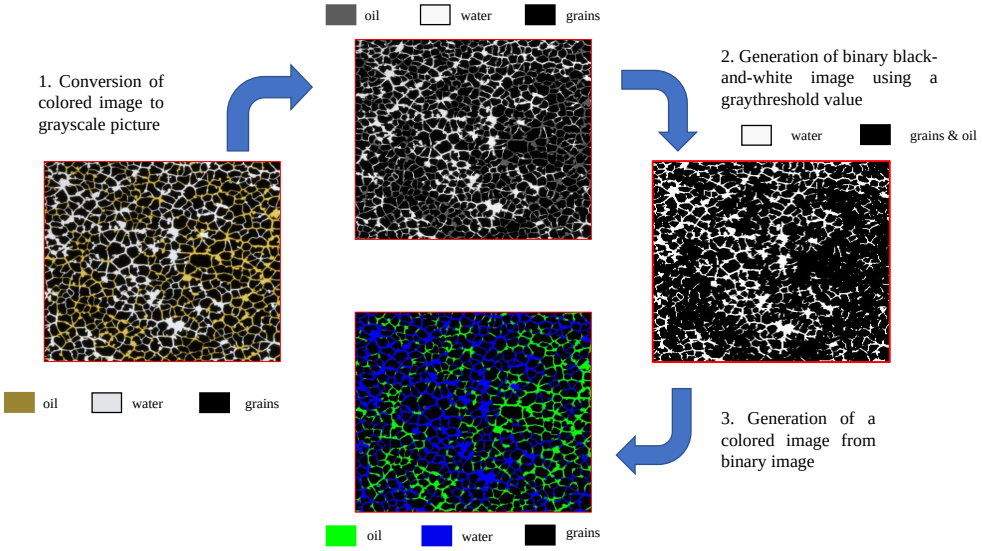

Figure 4. Procedure of converting the original image into a grayscale picture, followed by a binary image and developing the colored image. Simultaneously, the saturations were determined.

As shown in Figure 4, each image was read separately into the image processing tool MATLAB. An image processing code was written and generated, which was applied to every acquired image.

First, the original image was converted into a grayscale version (Step 1). In this grayscale image, the number of pixels representing the pore space was determined. Then, the number of pixels containing oil and water were determined, and the pixel numbers of water and oil were each divided by the previously computed total pore space. This provided the water and oil saturations in the micromodel. This was portrayed in the binary image, which was generated by applying a color thresholder to distinguish between the two liquid phases (Step 2). The developed algorithm also included a step to identify the saturations in a very thin pore throat. Analyzing the pore throats of interest involved determining the pixels of the picture and their respective values. Depending on whether the value of the pixel was below or above a certain graythresh value, that particular pixel represented either water or oil. Occasionally, in very thin pore throats, it is difficult to classify pixels as either representing water or oil. To address this uncertainty, a color thresholder was added to the algorithm to improve the distinction of pixels in narrow pore throats. The last step of the processing was to generate an image of the original one depicting oil in green and water in blue color (Step 3).

Further relevant parameters that were determined from the image analysis were the initial saturations of oil (S_{oi}) and water (S_{wi}), as well as the residual oil (S_{or}) and water (S_{wr}) saturations. During the analysis, the changes in the water (S_w) and oil saturation (S_o) were determined. The first flow rate of 0.03 µL/min was the main focus of image analysis as the immiscible displacement in the microchip and water breakthrough occurred during this laminar flow rate. The image analysis also provided the breakthrough time (t_{bt}) of the experimental water front. The breakthrough time indicated the time the flowing displacing front needed to flow through the entire micromodel and reach the end of the structure. Additionally, the parameters determined from the experiment were the waterfront saturation (S_{wf}) and the recovery factor RF. The images taken before and after the actual displacement process were used to determine the initial oil and water saturations (S_{oi} and S_{wi}) and the residual oil and water saturations (S_{or} and S_{wr}).

Furthermore, the images taken between the beginning of the inflow of the displacing water and the outflow were evaluated to visually determine the displacement process. Another step of the image analysis process was to determine the local water saturations in certain areas of the micromodel as the displacing front moved through it. This provided the spatial discretization of the water saturation in the chip. MATLAB was applied again to complete this task. Each image depicting the displacement process was divided into image segments, which all had the same size. Each segment showed an individual part of the micromodel. In every segment, the local water saturation was determined with the same method as it was for the entire microchip. This enabled the plot of the change in water saturation in certain time steps in local areas of the microchip.

The values of S_{or}, S_{wr}, S_{oi}, and S_{wi} determined by analyzing the images in MATLAB were the essential experimental values besides the RF. Furthermore, they were the basics for the development of the analytical solution for this experiment. Furthermore, both types of results were necessary to conduct the comparison of the solutions. The experimentally obtained values of S_{wf} and t_{bt} were compared to the analytically calculated counterparts.

2.5. Development of the Analytical Solution

The development of the analytical solution for this experiment was an essential step, which followed after the experiment. The experimentally determined values of S_{oi}, S_{wi}, S_{wr}, and S_{or} were applied to the calculation and development of the analytical result. The analytical frontal advance displacement was plotted, and the breakthrough time and the recovery factor (RF) were determined. The equations used to generate the displacement graphs (frontal advance displacement equation), the fractional flow curve equation, and the equation for the breakthrough time were applied. To develop the fractional flow curve, the fractional flow equation was used, which is shown in the following Equation (1):

$$f_w = \frac{1}{1 + \frac{k_{ro}}{k_{rw}} \cdot \frac{\mu w}{\mu o}} \tag{1}$$

f_w stands for the fractional flow of water (-); k_{ro} and k_{rw} indicate the relative permeability values of oil and water (-); μw and μo stand for the water and oil viscosities (mPas). The values of the relative permeabilities were calculated based on the Corey–Brooks model. The endpoints of the relative permeability curves for water and oil were determined from the experimental data provided in Section 2.3. The modified fractional flow equation was solved to calculate f_w for the range of water saturations between S_{wi} and S_{or}.

The values of S_{wi} and S_{wr} were not only used for the generation of the fractional flow curve. These parameters were also applied for the analytical frontal advance displacement graph. The fundamental equation used to develop the frontal advance displacement graph is the following Equation (2) [1,15,16]:

$$\frac{dx_{Sw}}{dt} = \frac{q_i}{A \cdot \phi} \frac{\partial f}{\partial S_w} \tag{2}$$

Equation (2) stated above indicates the velocity of a certain saturation at a certain time of the displacement process. The next step involved rearranging this equation in order to obtain a formula that enables the determination of the location of a particular saturation. The rearrangement is shown in the following Equation (3) [1,15,17]:

$$x_{Sw} = \frac{q_w \cdot t}{A \cdot \phi} \cdot \frac{\partial f_w}{\partial S_w} \quad (3)$$

x_{Sw} indicates the traveled distance of water (m); q_w is the injection rate (m^3/s); t is the time (s); A is the area (m^2); ϕ is the porosity (-); $\frac{\partial f_w}{\partial S_w}$ is the derivative of the fractional flow (-). With the help of the above equation, the location of a selected saturation at a particular time can be determined. For the analytical frontal advance displacement, this equation was applied to the saturations in the range from S_{wi} to S_{wr}.

3. Results and Comparison of the Experimental to the Analytical Solutions

As mentioned earlier, the goal of this paper is to validate the microchip by comparing the analytical and experimental solutions of an immiscible waterflooding process conducted in a micromodel. The analytical solution was derived from the Buckley–Leverett theory. The aspects to be compared were the breakthrough times and the displacement pattern. In addition to those two values, the parameters of S_{oi}, S_{wi}, S_{wr}, and S_{or} were determined. The calculated values can be seen in the following Table 1.

Table 1. Overview of the parameters determined from experimental results.

Mobility Ratio (M) (-)	S_{oi} (-)	S_{wi}(-)	S_{or} (-)	S_{wr} (-)	t_{Bt} (Seconds)	RF (-)
2.5	0.714	0.286	0.302	0.698	3840	0.57

The displacement pattern of the experimental and the analytical displacement front can be compared by examining and analyzing the frontal advance displacement graphs of the two solutions. The analytical and experimental frontal displacement fronts were plotted in MATLAB in one figure. This enabled a direct visual comparison of the two solutions. In order to compare the breakthrough times, the frontal advance displacement front equation was rearranged and solved to determine the breakthrough time.

3.1. Experimental Results

The results of the permeability measurement provided an average permeability of approximately 1930 Millidarcys (mD), which closely matched the designed permeability value (2000 mD). The results involved the calculation of the breakthrough time (t_{bt}) and the generation of the frontal advance displacement graph. The breakthrough time t_{bt} was determined based on the images that showed the waterfront entering the micromodel until it reached the end of the structure. The changes of the oil and water saturations during the displacement process were examined and analyzed with the image processing tool. The aspects to analyze were the changes in the saturations as the water injection continued and the front flowing through the micromodel. The following Figure 5 displays the changes in the water saturation as a function of water pore volume (PV) injected.

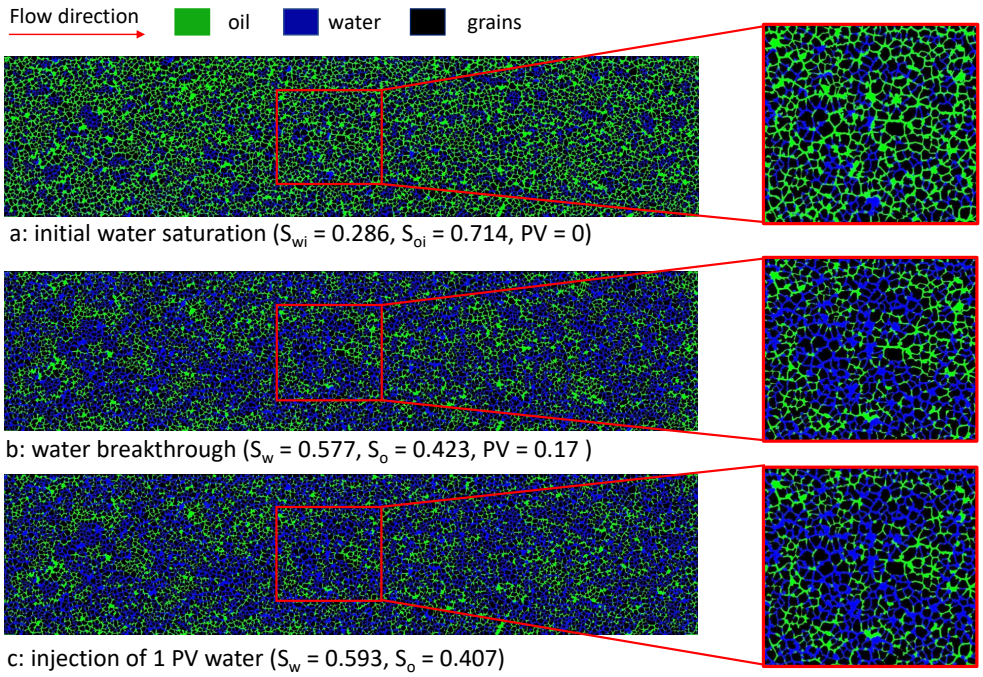

Figure 5. Development of the water saturation as a function of PV injected.

The above Figure 5 depicts how the waterflooding process changes the overall water saturation in the microchip. Before the displacing water enters the microchip, the saturations of both phases are at their initial values (Figure 5a) (S_{wi} = 0.286, S_{oi} = 0.714). At a constant rate of approximately 0.03 µL/min, the water enters the micromodel and starts filling the pores. As it moves on, it mobilizes the oil inside the pores. As the water displaces the oil and moves towards the microchip outlet, the oil saturation decreases while the water saturation increases. Figure 5b shows the oil and water saturations when the waterfront reaches breakthrough (S_w = 0.577, S_o = 0.423). Figure 5c shows the saturations after 1 PV was injected (S_w = 0.593, S_o = 0.407). The injection rate of 0.03 µL/min was continued until approximately 1.8 PV had been injected. Bump rates were implemented after the first injection rate was completed. The process of the bump rates was performed in order to develop the relative permeability curves of the water. The development of the pressure and water saturation during the entire waterflooding process is shown in the following Figure 6.

Figure 6a shows how the pressure and the global water saturation developed during the water injection. The water saturation increased from its initial value at approximately 0.3 up to slightly over 0.6 during the first injection rate of 0.03 µL/min. Then, the bump rates were performed to reach the residual oil saturation. As expected, the pressure increased by only approximately 200 mbar at the end of the second injection rate. During the bump rates, S_w increased as the injection rates were increased. At the end of the first injection rate (0.03 µL/min), based on the pressure differential, the calculated relative permeability endpoint for water was approximately 0.002. This value increased to around 0.022 at the end of the following injection rate (1 µL/min) due to the higher S_w. Therefore, the increase in the pressure drop was only two-times the first pressure drop even though the flow rate was increased by 30 times of the first injection rate. This would not have been the case in a single-phase flow. Furthermore, the increase in S_w during the second injection rate reduced significantly in comparison to the first flow rate. After the final flow rate, the water saturation remained stable, very close to the residual water level.

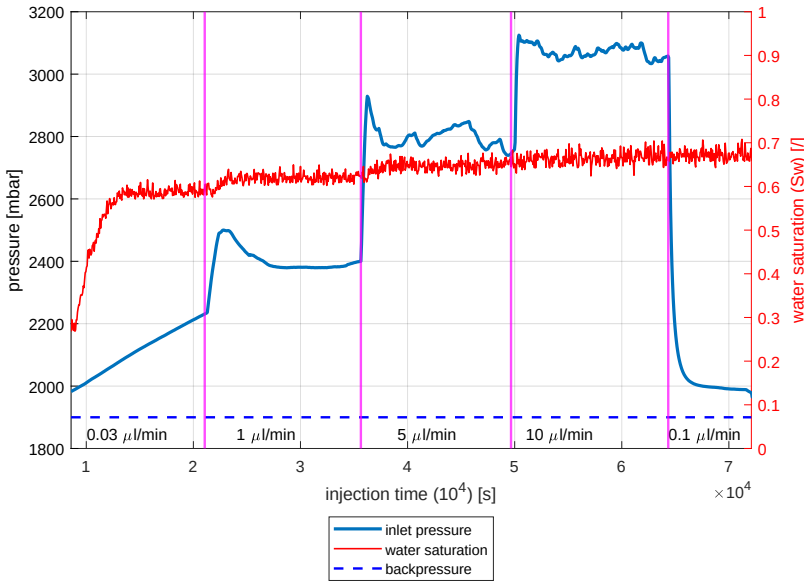

(**a**)

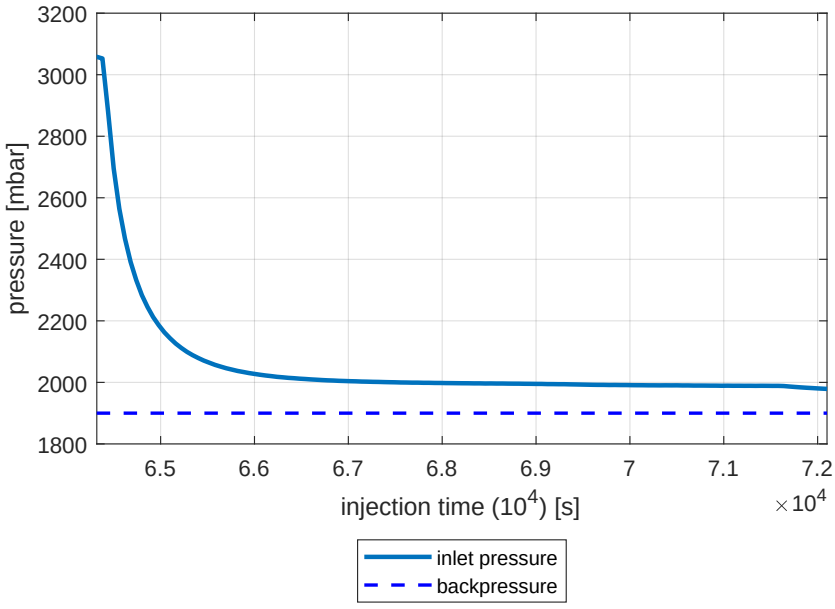

(**b**)

Figure 6. Development of the pressure and the water saturation in the micromodel during water injection. (**a**) depicts the development during the entire waterflooding process; (**b**) shows the pressure curve during the last flow rate of 0.1 µL/min.

Figure 6b depicts the change and stabilization in pressure during the last flow rate. This was needed for the calculation of the relative permeability endpoint of water, which will be mentioned in the next section.

To generate the frontal advance displacement graph, the number of images, showing the water displacement process in the micromodel, was relevant. It should be recalled that the time step between every image was 60 s and that it took slightly more than one hour for the water front to reach breakthrough. For this reason, certain time steps were chosen for the comparison between the analytical and experimental results. The chosen time steps were the moment the water entered the micromodel, the moment of breakthrough, and the front position mid-way through the microchip.

Spatial Discretization

For these time steps, the respective times were added to the plot to show the position of the front and the saturations in the micromodel. The images were divided into segments, which all had the same length. In each segment, the local saturations were determined in order to visualize the movement and the position of the displacing front. This process of image segmentation is visualized in the following Figure 7.

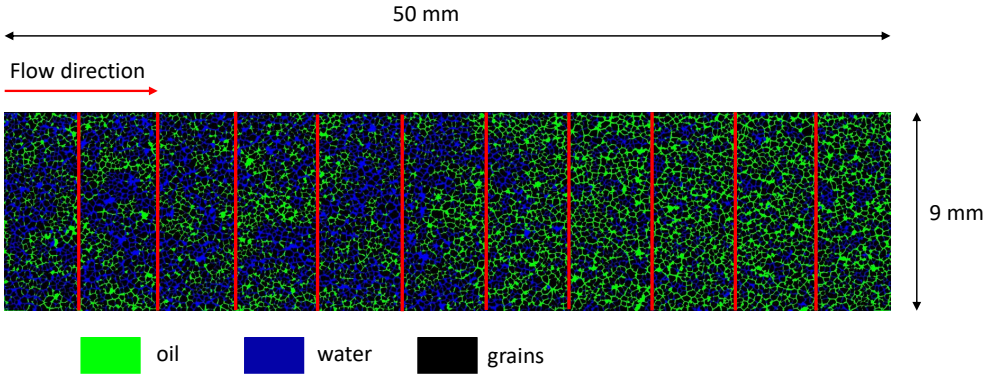

Figure 7. Image segmentation.

Figure 7 displays the water displacement process in the micromodel at t = 1320 s. Additionally, Figure 7 shows that one image was divided into eleven image segments; each segment had the same length. The number of segments covered the entire area of the micromodel. For every segment, the local saturations for oil and water were determined with MATLAB. The reason for selecting eleven image segments was that the local saturations in every segment were the closest to the representative element volume (REV). For comparison, the segmentation of the image into six and 21 parts was also performed, and the local water saturation in each segment was analyzed. At the selected time of 2040 s, the waterfront was intended to be approximately in the middle of the micromodel. The local water saturation values obtained in the different image segments were compared to each other as depicted in the following Figure 8.

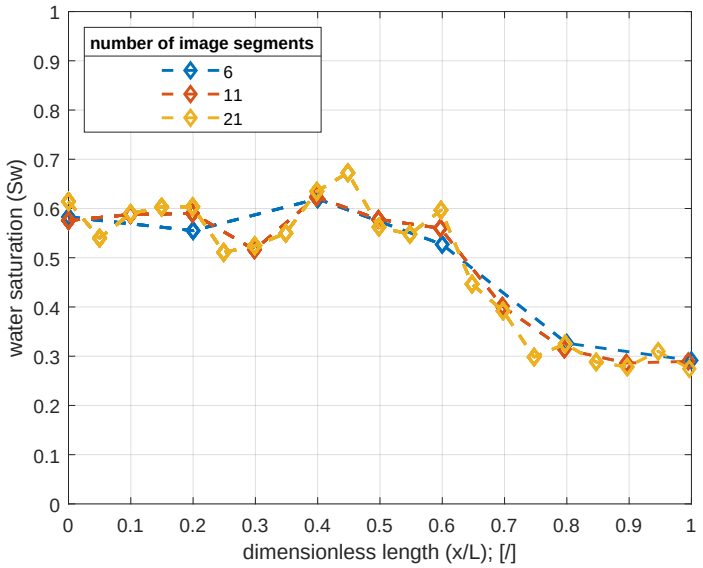

Figure 8. Local water saturation analysis for different numbers of image segments: the saturation distribution for six (blue), eleven (red), and 21 segments (yellow).

Figure 8 reveals that the local water saturations varied with the number of image segments. The blue line in Figure 8 shows the distribution of the local saturations when the image is divided into six equal segments. The development of the water saturation is nearly a smooth curve. The red and yellow lines depict the local saturations in eleven and 21 segments. The plots reveal that more segments lead to a better visualization of the position and the shape of the flowing front. In eleven segments, the position of the front is more distinct than in six segments, and in 21 segments, its location and shape are more noticeable than in eleven segments. Simultaneously, as the number of image segments increases, the fluctuations in the local saturation values intensify. The increase in fluctuations is based on the differences in the local values of porosity and S_w in every segment. If the segments reduce in size, then the local values of S_w increase. In six image segments, less fluctuations in saturation values are noticed than for eleven segments. The fluctuations increase when the number of image segments is raised to 21. The comparison reveals that the saturations in eleven image segments are the closest to picturing the position of the flow front, which was validated by comparison through global saturation changes. Additionally, the curve is much smoother, and the shape of the lines is much more even. Furthermore, the analysis revealed that the local saturations in this case were much closer to the representative elementary volume (REV). For these reasons, the image analysis was conducted with a segmentation number of eleven.

The process of image segmentation was performed for the images depicting the waterfront moving through the micromodel in the conducted experiment. The values of the obtained local water saturations are plotted as shown in the following Figure 9.

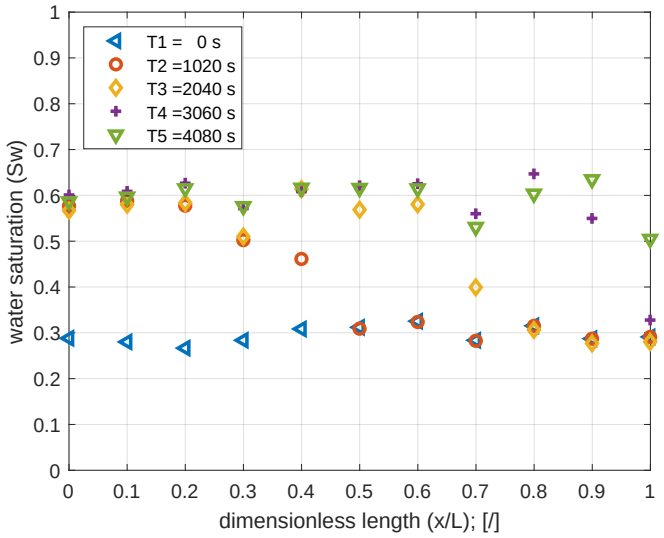

Figure 9. Experimental frontal advance displacement (M = 2.5).

Figure 9 shows the distribution of the local water saturations during waterflooding through the entire micromodel between the initial state and approximately the breakthrough time. The y-axis shows the values of the water saturations, and the x-axis indicates the position in the micromodel in a dimensionless form.

The frontal advance displacement shows the change in the water saturation over time and the location of the displacing front in the microchip. The image analysis concluded that the time of breakthrough (t_{bt}) was slightly more than 3600 s. At approximately this time, a noticeable increase in the water saturation was detected at the outflow of the micromodel. The flow of the waterfront through the micromodel is clearly noticed in the plot. For the time steps of 1020 s and 2040 s, the difference in the water saturation between two image segments around the center area of the micromodel is noticed. Additionally, the saturations behind the flood front for the time steps T2 and T3 are at nearly the same level.

3.2. Analytical Results

To generate the analytical solution, the experimentally determined values of S_{oi}, S_{wi}, S_{or}, and S_{wr} (Table 1) were applied. In this subsection, the analytical fractional flow curve of water (fw) was also generated. In this experiment, only two phases flowed during the displacement process: water and oil. Figure 10 shows the relative permeability curves with the endpoints and the analytical fractional flow curve of this experiment.

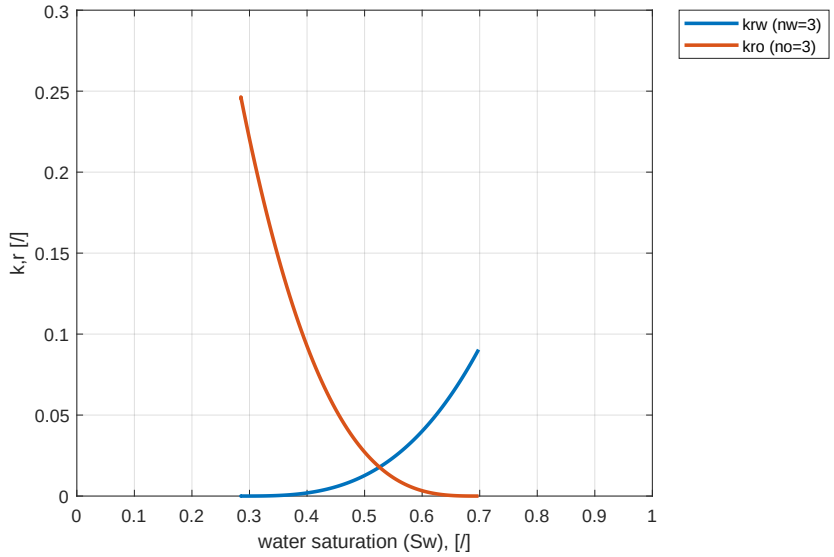

(**a**)

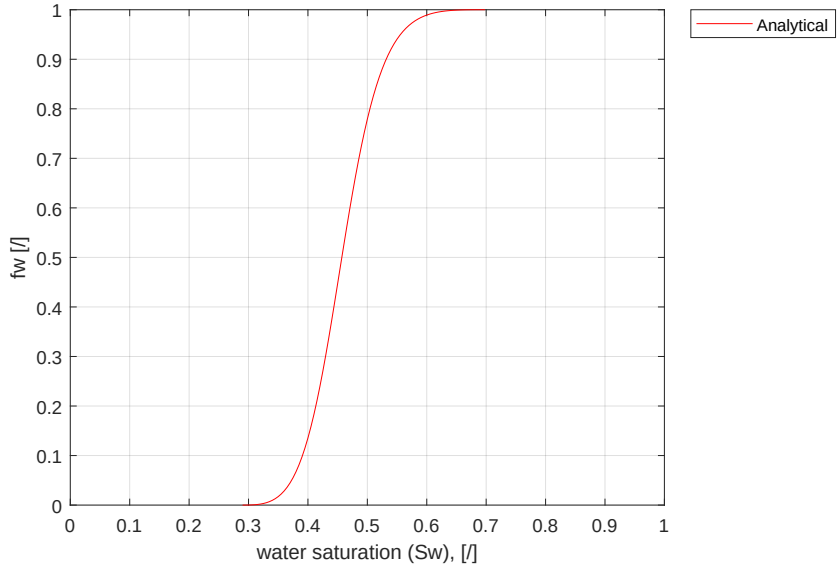

(**b**)

Figure 10. Relative permeability curves of oil and water during waterflooding (**a**); the fractional flow curve of water (**b**).

The above Figure 10 shows the relative permeability curves (Figure 10a) and the fractional flow of water as it moves through the micromodel (Figure 10b). The portrayed relative permeability curves were used as the input to generate the fractional flow curve. The endpoints of the flow curves were calculated from the final injection rate of the respective fluids. For instance, in Figure 10a, the water endpoint was calculated with the pressure data obtained from the last water flow rate shown in Figure 6b. The same approach was applied for the oil relative permeability curve. The relative permeability curves influence

the shape of the fractional flow curve. The latter starts at its initial saturation value and ends at the residual saturation value (S_{wr}). The shape of the curve reveals that it has the shape of an "S". This shape is considered optimal when it comes to describing the behavior of the flow of the fluid during the displacement process. For this analytical result, this is an indicator that the performed calculation was appropriate and that the result is acceptable. The plot of the analytical FAD is depicted in the following Figure 11.

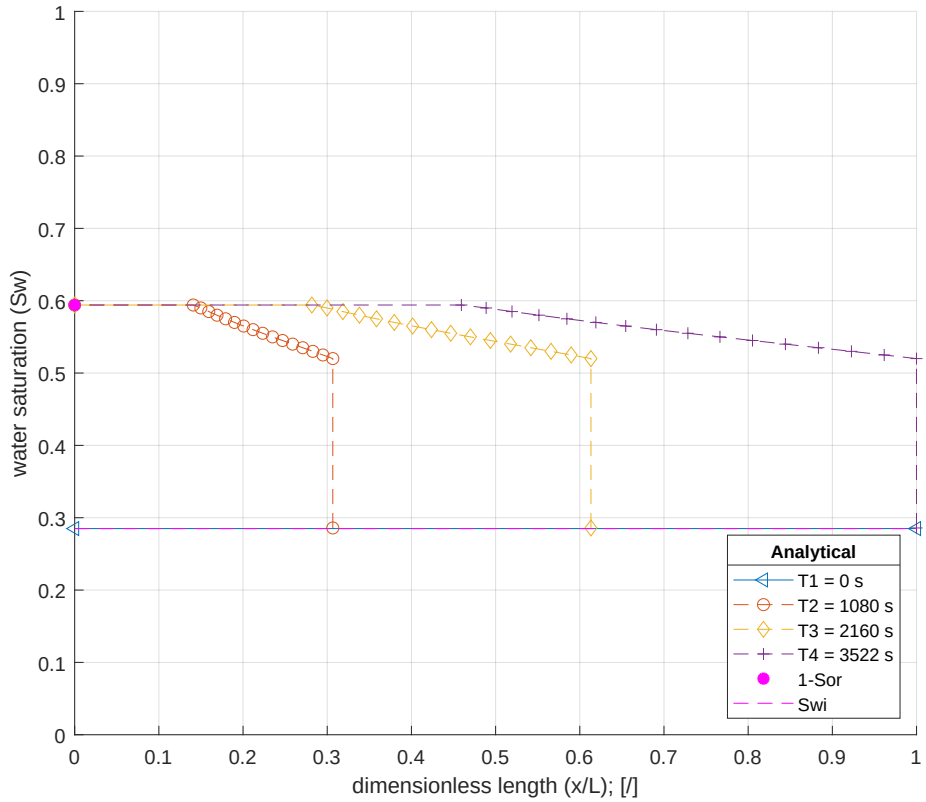

Figure 11. Analytical frontal advance displacement (M = 2.5).

Figure 11 shows that at T1, just before the entry of the displacing water into the micromodel, the saturation of water and oil in the chip should be evenly distributed. This is shown as the light pink dotted line. After T1, a constant water front saturation (S_{wf}) develops at a water saturation of approximately 0.52 at the inlet of the microchip. As it moves through the micromodel, it maintains this saturation level and exits the micromodel at that same value. The plot shows a clear shock front and a clear rarefaction wave of the flood front. Furthermore, the analytical breakthrough time was determined to be approximately 3522 s.

The analytical Buckley–Leverett equation shows the ideal behavior of the immiscible displacement. The analytical frontal advance displacement graph should resemble this flooding behavior. The water saturation has a stable and an unstable part. The unstable part is a slow, non-linear decline until the front saturation is reached. This is characterized by a shock. This shock front indicates the saturation at which the displacing fluid flows through the porous media, and it is utilized to determine the breakthrough time t_{Bt}.

3.3. Comparison of the Experimental and the Analytical Solution

The principal aspect of this paper is the comparison of the analytical to the experimental solution. After determining the frontal advance displacement process in both results, a direct comparison between the two solutions in this subsection follows. The following Figure 12 is a depiction of this comparison. The experimental values are pictured as symbols, and the analytical values are shown as lines.

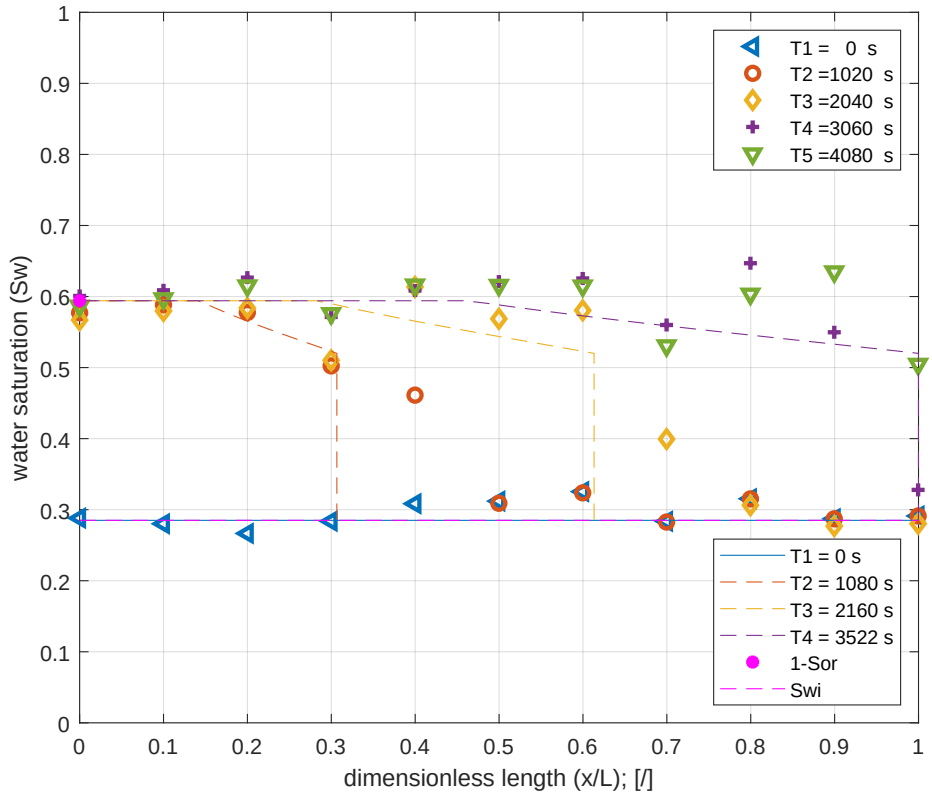

Figure 12. Comparison of the analytical and experimental frontal advance displacement graphs (M = 2.5).

The comparison of the experimental to the analytical solution in Figure 12 reveals common aspects and some noticeable differences. The analytical shapes of the curves indicate an ideal behavior of the fluids as the displacing fluid moves through the porous media. Furthermore, the analytical curves for the various time steps show the rarefaction wave and the shock front of the displacing fluid and its position inside the micromodel. According to the analytical solution, the breakthrough time t_{Bt} was calculated to be approximately 3522 s, and the experimental results showed that t_{Bt} was approximately 3840 s. This indicates an acceptable match between the two results. However, as expected, the experimental results showed that the water saturation in the image segments does not have a piston-like displacement front as it permeates through the micromodel. In certain areas of the micromodel, the local initial water saturation exceeds the average value of S_{wi}. The experimental results showed the areas in which the water saturation changed with time. Between the time steps of T2 (1020 s) and T3 (2040 s) in the experiment, the changes in the water saturation are identified in the plot. Additionally, the analytical saturation values of those two time steps were also compared. Even though the experimental solution did not show a clear rarefaction front due to the effects of spatial discretization, a significant change in the saturations can be seen at those two time steps. The observation of the experimental water saturation values between those two time steps showed the position of the water front during its displacement.

The comparison revealed that the analytical solution depicts the ideal behavior of the immiscible displacement, while the experimental results represent the actual real-life behavior of immiscible displacement processes. The mentioned differences did not have a great influence on the other essential parameters. In this experiment, the values of t_{bt} and S_{wf} were nearly identical and the deviations were negligible. The generated analytical solution covered the displacement process in the microchip as one complete part. Due to the procedure of image segmentation, local results were obtained. Normally, an analytical solution can be developed for every individual segment. This would have been used to

compare it to the experimentally determined local saturations. This procedure might have concluded an even better match between the two results. Another aspect to be mentioned was the calculation of the relative permeability. For the generated analytical solutions, the model of Corey–Brooks was applied as shown in Section 2.5 (Development of the Analytical Solution). The question arises how another relative permeability concept would have shaped the analytical results and how those would have matched the experimental solution. However, the two mentioned aspects were not applied in this experiment due to limited time.

4. Discussion

In this paper, an immiscible displacement experiment was conducted with a microchip, which was developed by applying a new method. An original reservoir sandstone core was scanned and a multiple 3D image stack portraying the examined section of the core was generated. The 3D image stack was used as the model to fabricate the microchip, which replicates the obtained reservoir properties. In particular, the microchip remodeled the permeability, porosity, and grain size distribution in a Bentheimer core. These features indicated that the conducted displacement experiments were subject to real-life reservoir influences, and this permitted a better understanding of the fluid behavior in reservoir rocks. Additionally, analytical solutions were generated and compared to the obtained results of the carried out immiscible displacement experiments.

4.1. Fingering Effect

In the conducted experiment, the value of the mobility ratio (M) was greater than two. If an immiscible displacement process has a mobility ratio greater than one, it is considered to be an unstable displacement. In cases like these, the displacing fluid moves quicker than the displaced fluid. During the process, the displacing fluid will bypass the displaced one and the former will reach the outflow earlier. This indicates that the experiment was an unstable displacement process. The reason for unstable displacement is the difference in viscosity between the displacing and the displaced fluid. The viscosity of the displacing fluid is lower than the viscosity of the displaced fluid, which means that the type of instability was viscous instability [18], which is also known as the Saffman–Taylor instability [19]. In the fingers, the velocity of the displacing fluid is at its maximum. In the conducted experiment, distilled water had a viscosity of μ_w = 1 cP and oil had a viscosity of μ_o = 7.55 cP at room temperature. This difference in viscosity led to the development of viscous fingers [20]. The displaced oil arrived at the outflow later. The analysis of the images with the image processing tool revealed that the displacing water formed viscous fingers during the waterflooding process, which confirmed the instability of the experiment. In the fingers, the water moved quicker than the oil, and the water in the viscous fingers reached the outlet of the micromodel earlier [9,19,20].

It should be recalled that the capillary pressure was neglected to simplify the comparison of the experimental to the analytical results. However, as two phases were present in the micromodel during the experiment, capillary pressure should be considered. Capillary pressure might have some influence on the results, which should be considered in future immiscible displacement experiments with micromodels. When the micromodel was saturated with oil, the process was a drainage process as the non-wetting oil was injected into a water wet micromodel. For the oil to start filling the pores, the injection pressure needed to overcome a threshold pressure. During waterflooding, the wetting fluid displaces the non-wetting fluid (oil) in the pores. This process is defined as imbibition. The general depiction of the capillary pressure during drainage and imbibition and the development of the differential pressure during oil initialization in the micromodel are shown in the following Figure 13. The red circles in both figures indicate the possible capillary threshold pressure during the drainage process.

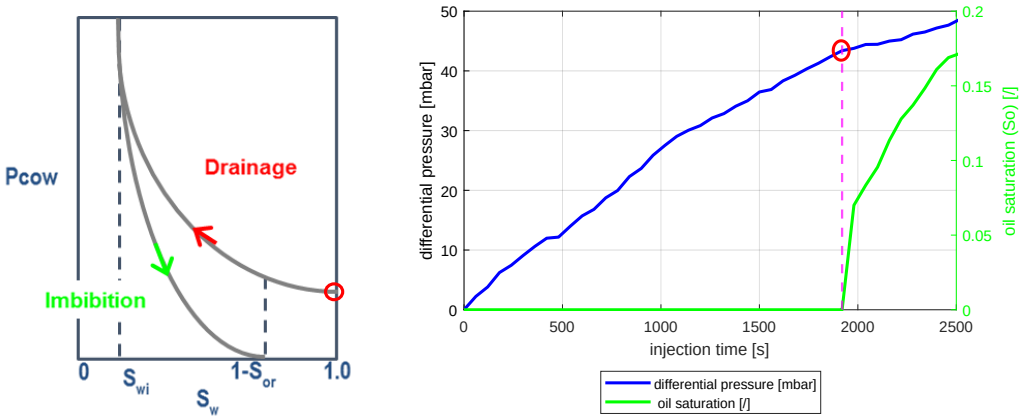

(**a**) (**b**)

Figure 13. Typical drainage and imbibition curves (**a**); the development of differential pressure and oil saturation during initial oil flooding in the micromodel (**b**).

Figure 13a shows the typical drainage and imbibition curves. It also indicates that there is a certain threshold pressure during the drainage process. This is the pressure level that the injection pressure has to overcome to start filling the porous media with the non-wetting fluid. After exceeding the threshold pressure, the oil saturation and the pressure values increase. During imbibition, such a threshold pressure is not expected as the wetting fluid starts to fill the pores. In Figure 13b, the development of the oil saturation (green) and the differential pressure (blue) in the micromodel during oil initialization are depicted. Figure 13b reveals that between 0 and 1920 s of injection time, the differential pressure increases, but there is no increase in oil saturation. Just after a 1920 s injection time, the oil saturation begins to increase. The respective differential pressure at that time indicates the threshold pressure for oil to enter the porous media. The development of the differential pressure and the oil saturation suggest that capillary pressures were likely to be present in the micromodel during the experiment. The capillary pressures would also influence the results of the flooding experiments. These pressures and their influences can be the focus of future and more extensive micromodel experiments.

4.2. Breakthrough Time

Further differences were noticed in the frontal advance displacement graphs of the experiment and the analytical results. The analytical solution describes the theoretical behavior of the immiscible displacement process. It presumes that the waterfront permeates at a constant saturation through the micromodel from the inlet all the way until the outlet at every time step. This theoretical behavior is also depicted in the frontal advance displacement graphs. In this experiment, the analytical water saturation front (S_{wf}) was approximately 0.52, which should form at the inlet of the micromodel and last until the outflow was reached. However, the experimental results indicated no steady waterfront saturation. Due to the development of the viscous fingers, the displacing water entered certain porous areas earlier than others. The others were flooded with water later after the viscous fingers moved further. In this case, a uniform displacement front did not form starting at the inlet. Despite the previously mentioned viscous instability and the formation of viscous fingers, these did not significantly alter the t_{Bt} of the displacing fluid. The result of the experimental t_{bt} (3840 s) and the analytical t_{bt} (3522 s) solutions were very close to each other. The comparison of the displacement graphs revealed that the positions of the analytically determined and the experimental waterfront at the selected time steps were at nearly identical positions in the micromodel. For instance, the position of the analytical front at half of the breakthrough time was in close proximity to the experimental front (Figure 12). The figure shows that the dimensionless location of the analytical front was between 0.6 and 0.7, while the experimental front was also in that particular image segment.

4.3. Image Analysis

Another crucial aspect was to conclude whether the application of the developed algorithm for image processing and the conduction of immiscible displacement experiments in a microchip, which was fabricated using a new method, led to solid results. The microfluidic device with the same setup was used for similar waterflooding experiments before [11,12]. The visualization of the experiment was completed with a micromodel replicating the internal porous structure of a Bentheimer sandstone core. As the comparison of the experimental to the analytical solution revealed, the match of the two types of results was good and the deviations were negligible. The values of the breakthrough times and the positions of the waterfront were close to each other. This implied that the overall setup and procedure of the experiments were conducted properly. The good match of the results could also be connected to the calculation of the relative permeability endpoints for both phases and its implementation in the analytical solution. The determination of the endpoints derived from experimentally obtained values was shown in the subsection Experimental Procedure. This was essential because it helped to calculate the analytical results, which meant that the relative permeability calculation was not purely analytical. This influenced the shape of the fractional flow curve. Additionally, the development of the algorithm for the image processing tool, which assisted in determining the overall and local saturation values, delivered valuable results. The application of the algorithm to distinguish water from oil in very narrow pore throats also contributed to the results. The essential displacement parameters were considered in the analytical part of this paper. As these parameters matched the experimentally observed results, it can be concluded that the brand new micromodel used is an outstanding tool to perform upscaling of flow properties from microfluidic to reservoir rock [11]. This micromodel can be used to observe the influences of reservoir rock properties on the flow behavior of the fluids.

5. Conclusions and Outlook

The theory of Buckley–Leverett is a useful approach to describe the immiscible displacement process of two incompressible fluids when the flow of the fluids occurs in one direction and the capillary pressure is neglected. The goal of this paper was to carry out a validation of a brand-new microchip replicating the internal structure of a reservoir sandstone by using a Buckley–Leverett approach and evaluating key displacement parameters. The displacement experiments were conducted in a glass–silicon–glass micromodel, which possessed a replicated internal structure and characteristics of a Bentheimer sandstone reservoir core. The experimental process was to inject water as a displacing fluid to mobilize the initial oil in place and observe the displacing behavior. The analysis of the two types of solutions disclosed that the analytically determined time for the water to flow through the micromodel was close to the experimental time. Similar results were obtained for the development of the water saturation in the microchip and the permeation of the waterfront. Slight deviations in the values of local saturations were noticed. However, these did not have a major influence on the results. Noticeable differences occurred in the comparison of the frontal advance displacement graphs. The displacement process was considered unstable as the mobility ratio was greater than one. The experimental solutions showed that the structure of the displacing front was not even. This indicated the development of viscous fingers, which were the result of the viscosity difference between the displacing and the displaced fluid. Still, the locations of the analytical and the experimental waterfronts during the flow were also very close to one another. This indicates that the comparison of the relevant parameters suggests that the fluid front propagation in micromodels was in agreement with the Buckley–Leverett theory. The newly applied methodology of constructing micromodels, which represent a part of the porous structure of a real core, was proven precise and useful. Furthermore, the real structure micromodel contributed to the understanding of the fluid behavior in porous media. The experimental results verified that the experimental procedure was conducted appropriately. The results also implied

that the development and the implementation of the new image processing algorithm to obtain essential parameters proved very useful and provided good results.

An important aspect for future experiments is capillary pressure. During two-phase displacement experiments, capillary pressures usually influence the flow behavior of the flowing fluids. For every porous medium, the drainage and imbibition curves are individual. To understand the influence of capillary pressure on the fluid flow, these curves for the respective porous media need to be developed. To accomplish this and to determine capillary threshold values, future experimental setups could be amended by including an inline porous filter (similar to a porous plate used in core flooding) very close to the micromodel. The experiment conducted in this paper was a one-dimensional displacement process. Further experiments should consider all three dimensions in rock properties. Three-dimensional experiments should focus on the mobilization of trapped oil ganglia. Datta et al. performed mobilization experiments on 3D models and observed the behavior of oil ganglia under the influence of capillary and viscous forces [21]. During that process, experimental models were developed, and these can be further amended, as well as analytical models. Further investigation should focus on other relative permeability approaches to fluid flow behavior in micromodel applications. The usage of micromodels to visualize fluid flow behavior in porous media is very promising and should be intensified.

Author Contributions: C.T.L. performed the two-phase immiscible displacement experiments, defined the methodology, and conducted the evaluation of the outcome of the experiments. Additionally, he generated the analytical solution. C.L.G. performed the experiments and reviewed and performed the editing. G.J.S. and L.G. conducted a review and edited the text. All authors have read and agreed to the published version of the manuscript.

Funding: The authors acknowledge support by the Open Access Publishing Fund of the Clausthal University of Technology.

Institutional Review Board Statement: Not applicable.

Informed Consent Statement: Not applicable.

Data Availability Statement: The data presented in this study may be made available upon request.

Conflicts of Interest: The authors declare no conflict of interest.

Abbreviations

The following abbreviations are used in this manuscript:

A	area
FAD	frontal advance displacement
μCT	micro-computer tomography
mD	Millidarcy
f_w	fractional flow of water
k_{rw}	relative permeability of water
k_{ro}	relative permeability of oil
q_i	injection rate
S_{oi}	initial oil saturation
S_{or}	residual oil saturation
S_{wi}	initial water saturation
S_{wr}	residual water saturation
t_{Bt}	breakthrough time
ϕ	porosity
x_{Sw}	traveled distance of a water saturation
μw	viscosity of water
μo	viscosity of oil

References

1. Buckley, S.E.; Leverett, M.C. Mechanism of Fluid Displacement in Sands. *Trans. AIME* **1942**, *146*, 107–116. [CrossRef]
2. Babson, E.C.; Sherborne, J.E.; Jones, P.H. An Experimental Water-flood in a California Oil Field. *Trans. AIME* **1945**, *160*, 25–33. [CrossRef]
3. Breston, J.N.; Hughes, R.V. Relation Between Pressure and Recovery in Long Core Water Floods. *J. Pet. Technol.* **1949**, *1*, 100–110. doi: 10.2118/949100-G. [CrossRef]
4. Johnston, N.; van Wingen, N. Recent Laboratory Investigations of Water Flooding in California. *J. Pet. Technol.* **1953**, *5*, 219–224. [CrossRef]
5. Talash, A.W.; Crawford, P.B. Experimental Flooding Characteristics of Unconsolidated Sands. In Proceedings of the All Days. SPE Permian Basin Oil Recovery Conference, Midland, TX, USA, 4–5 May 1961; p. 05041961. [CrossRef]
6. Zhang, T.; Sun, S. Thermodynamics-Informed Neural Network (TINN) for Phase Equilibrium Calculations Considering Capillary Pressure. *Energies* **2021**, *14*, 7724. doi: 10.3390/en14227724. [CrossRef]
7. Zhang, T.; Sun, S. A coupled Lattice Boltzmann approach to simulate gas flow and transport in shale reservoirs with dynamic sorption. *Fuel* **2019**, *246*, 196–203. [CrossRef]
8. Chatenever, A.; Calhoun, J.C. Visual Examinations of Fluid Behavior in Porous Media—Part I. *J. Pet. Technol.* **1952**, *4*, 149–156. doi: 10.2118/135-G. [CrossRef]
9. Kargozarfard, Z.; Riazi, M.; Ayatollahi, S. Viscous fingering and its effect on areal sweep efficiency during waterflooding: An experimental study. *Pet. Sci.* **2019**, *16*, 105–116. [CrossRef]
10. Wegner, J.; Hincapie, R.E.; Födisch, H.; Ganzer, L. Novel Visualisation of Chemical EOR Flooding Using a Lab-on-a-Chip Setup Supported by an Extensive Rheological Characterisation. In Proceedings of the SPE Asia Pacific Enhanced Oil Recovery Conference, Kuala Lumpur, Malaysia, 11–13 August 2015. [CrossRef]
11. Gaol, C.L.; Wegner, J.; Ganzer, L. Real structure micromodels based on reservoir rocks for enhanced oil recovery (EOR) applications. *Lab A Chip* **2020**, *20*, 2197–2208. [CrossRef] [PubMed]
12. Tahir, M.; Hincapie, R.E.; Langanke, N.; Ganzer, L.; Jaeger, P. Coupling Microfluidics Data with Core Flooding Experiments to Understand Sulfonated/Polymer Water Injection. *Polymers* **2020**, *12*, 1227. [CrossRef] [PubMed]
13. Tahir, M.; Hincapie, R.E.; Gaol, C.; Säfken, S.; Ganzer, L. Describing the Flow Behavior of Smart Water in Micromodels with Wettability Modified Pore Structures. In Proceedings of the SPE Latin American and Caribbean Petroleum Engineering Conference, Virtual, 27–31 July 2020: p. 07272020. [CrossRef]
14. Gaol, C.L.; Ganzer, L.; Mukherjee, S.; Alkan, H. Parameters govern microbial enhanced oil recovery (MEOR) performance in real-structure micromodels. *J. Pet. Sci. Eng.* **2021**, *205*, 108814. [CrossRef]
15. PermInc TIPM Laboratory: Buckley–Leverett Theory. *Immiscible Displacement—Buckley–Leverett Theory*; 2020. Available online: https://perminc.com/resources/fundamentals-of-fluid-flow-in-porous-media/chapter-4-immiscible-displacement/buckley-leverett-theory/ (accessed on 9 September 2022).
16. Wegner, J. Investigation of Polymer Enhanced Oil Recovery (EOR) in Microfluidic Devices that resemble Porous Media: An Experimental and Numerical Approach. Ph.D. Thesis, Clausthal University of Technology, Clausthal-Zellerfeld, Germany, 2015.
17. Ahmed, T.H. *Reservoir Engineering Handbook*, 5th ed.; Gulf Professional Publishing: Amsterdam, The Netherlands, 2018.
18. Saffman, P.G. Viscous fingering in Hele-Shaw cells. *J. Fluid Mech.* **1986**, *173*, 73–94. [CrossRef]
19. Panfilov, M. *Physiochemical Fluid Dynamics in Porous Media: Applications in Geosciences and Petroleum Engineering*; Wiley-VCH, Weinheim, Germany, 2019.
20. Kueper, B.H.; Frind, E.O. An overview of immiscible fingering in porous media. *J. Contam. Hydrol.* **1988**, *2*, 95–110. [CrossRef]
21. Datta, S.S.; Ramakrishnan, T.S.; Weitz, D.A. Mobilization of a trapped non-wetting fluid from a three-dimensional porous medium. *Phys. Fluids* **2014**, *26*, 022002. [CrossRef]